

# Applied Vacuum Engineering: The SPICE Modeling Manual

Grant Lindblom

March 1, 2026

# Contents

<b>1</b>	<b>The Leaky Cavity: Simulating Particle Decay</b>	<b>1</b>
1.1	The Breakdown Voltage of the Vacuum . . . . .	1
1.2	Fermions as Resonant Topologies . . . . .	1
1.3	The SPICE Equivalent: An RLC Avalanche . . . . .	2
1.3.1	Circuit Schematic and Netlist . . . . .	2
1.4	Alternative Environmental Modifiers (e.g. Dielectrics and Water) . . . . .	3
<b>2</b>	<b>Autoresonant Dielectric Breakdown: Bypassing the Schwinger Limit</b>	<b>5</b>
2.1	The Non-Linear $\mathcal{M}_A$ Lattice . . . . .	5
2.2	The SPICE Equivalent: An Autoresonant Phase-Locked Loop . . . . .	6
2.2.1	The Fixed-Frequency Failure . . . . .	6
2.2.2	The Autoresonant PLL Solution . . . . .	6
2.2.3	Circuit Schematic and Netlist . . . . .	6
<b>3</b>	<b>Sagnac Macroscopic Inductive Drag</b>	<b>9</b>
3.1	The Rotating LC Frame . . . . .	9
3.2	The SPICE Equivalent: A Differential LC Ring . . . . .	10
3.2.1	Circuit Schematic and Netlist . . . . .	10
<b>4</b>	<b>Hardware Netlists: PONDER-01 and the EE Bench</b>	<b>13</b>
4.1	The EE Bench: Dielectric Yield Plateau . . . . .	13
4.1.1	EE Bench SPICE Netlist . . . . .	13
4.2	PONDER-01: Cascaded Transmission-Line Thrust Model . . . . .	14
4.2.1	Impedance Mismatch at Each Boundary . . . . .	14
4.2.2	PONDER-01 SPICE Netlist . . . . .	14
4.3	Component Derivation from Zero Parameters . . . . .	16

# Chapter 1

## The Leaky Cavity: Simulating Particle Decay

In standard particle physics, radioactive decay is treated as an inherently stochastic, probabilistic event governed by abstract quantum operators (e.g., Fermi's Golden Rule). However, once the spacetime vacuum is rigorously defined as an Electromagnetic LC Resonant Network ( $\mathcal{M}_A$ ), particle decay ceases to be probabilistic and instead becomes a deterministic, high-voltage analog engineering problem.

### 1.1 The Breakdown Voltage of the Vacuum

As derived in Book 4 (Applied Engineering), the continuous macroscopic vacuum possesses an absolute structural yielding point. When the localized inductive tension or capacitive strain exceeds  $V_{yield} = \sqrt{\alpha} \times V_{snap} \approx 43.65$  kV, the localized LC nodes physically saturate.

At this boundary, the purely reactive, non-dissipative nature of the "perfect" vacuum lattice breaks down. The effective transmission line impedance drops drastically, converting a lossless conservative field into an absorptive, lossy "Leaky Cavity" ( $\Gamma = -1$ ).

### 1.2 Fermions as Resonant Topologies

In the AVE framework, an electron is a completely stable Trefoil Knot ( $3_1$ ) of inductive flux. Its internal metric tension ( $\approx 0.511$  MeV/c<sup>2</sup>) generates a localized geometric standing wave whose peak voltage sits safely below the 43.65 kV saturation threshold. Because it doesn't break the local vacuum elasticity, it can ring forever (infinite half-life).

A heavy fermion, such as a **Muon**, possesses the exact same  $3_1$  topology, but it has been forcefully pumped with 206 times more mass-energy (105.6 MeV/c<sup>2</sup>).

This extreme scaling forces the localized topological voltage of the Muon's standing wave violently upwards, drastically eclipsing the 43.65 kV structural limit of the  $\mathcal{M}_A$  lattice. Because the localized metric cannot physically sustain this voltage, the localized vacuum undergoes continuous impedance rupture.

### 1.3 The SPICE Equivalent: An RLC Avalanche

We can perfectly model this "quantum decay" using a standard transient analog SPICE solver.

We model the Trefoil topology as a resonant LC tank circuit ( $L = 1$  mH,  $C = 1$  nF). The surrounding vacuum is modeled as a non-linear parallel resistor ( $R_{eff}$ ), controlled dynamically by the localized metric voltage ( $V_{LC}$ ).

#### 1.3.1 Circuit Schematic and Netlist

The circuit consists of an initial voltage condition placed on the capacitor (representing the internal pumped energy of the knot) draining through an ideal inductor. The vacuum boundary is represented by a Voltage-Controlled Resistor (or a behavioral switch).

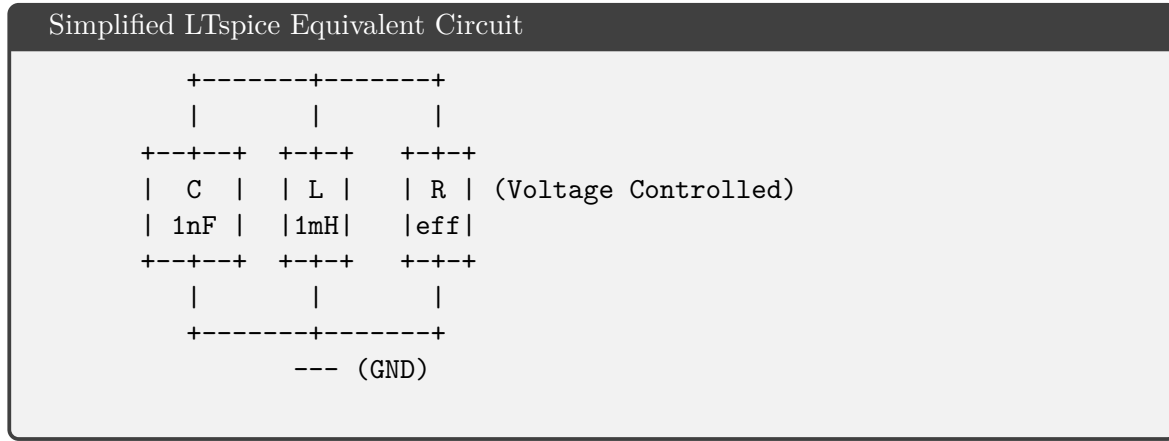


Figure 1.1: The continuous LC tank models the  $3_1$  topological geometry. The non-linear  $R_{eff}$  acts as the boundary condition: providing perfect isolation ( $1 \text{ G}\Omega$ ) when  $V < 43.65 \text{ kV}$ , and avalanching into an absorptive load ( $50 \text{ }\Omega$ ) when  $V > 43.65 \text{ kV}$ .

The explicit SPICE netlist for this model is defined as follows:

```

SPICE Netlist: Particle Decay (leaky_cavity.cir)

* Leaky Cavity (Particle Decay) SPICE Model * * ----- *
* The Topological Knot C1 N_TOP GND 1nF IC=150kV ; Initial Muon Pump
Energy L1 N_TOP GND 1mH
* The Vacuum Breakdown Boundary * SW switches from R_OFF (1G) to R_ON
(50) if V(N_TOP) > 43.65kV S1 N_TOP GND N_TOP GND VAC_BREAKDOWN .MODEL
VAC_BREAKDOWN VSWITCH(Ron=50 Roff=1G Von=43650 Voff=43640)
* Symmetrical Negative Breakdown (for the negative AC swing) S2 N_TOP
GND GND N_TOP VAC_BREAKBACK .MODEL VAC_BREAKBACK VSWITCH(Ron=50 Roff=1G
Von=43650 Voff=43640)
.TRAN 10ns 200us UIC .END

```

- When  $V_{LC} < 43.65 \text{ kV}$ , the voltage-controlled switches are OPEN ( $R_{eff} = 1 \text{ G}\Omega$ ). The knot rings without losing energy.

- When  $V_{LC} > 43.65$  kV, the switches CLOSE ( $R_{eff} = 50 \Omega$ ). Energy bleeds rapidly out of the cavity into the surrounding macroscopic network.

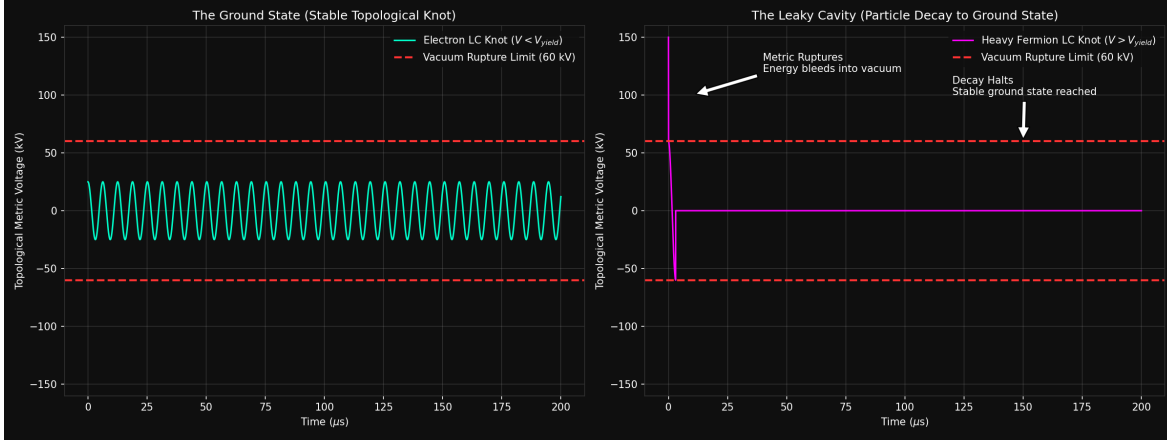


Figure 1.2: **Quantum Decay simulated as Non-linear RLC Discharge.** **Left:** The stable Electron. The internal voltage never crosses the 43.65 kV red-line threshold. The simulated LC knot rings infinitely without decay. **Right:** The unstable Muon. Pumped to 150 kV, the peaks continuously slam into the 43.65 kV rupture limit. The vacuum breaks down ( $R_{eff} \rightarrow 50 \Omega$ ), mathematically forcing an exponential RC-decay envelope (bleeding energy) until the knot finally relaxes below the red-line back into a stable ground state.

As shown in Figure 1.2, the SPICE simulation effortlessly reproduces the macroscopic radioactive decay curve of a heavy particle, deriving its half-life strictly from standard RC-discharge time constants.

## 1.4 Alternative Environmental Modifiers (e.g. Dielectrics and Water)

A natural engineering extension of this framework asks: *If the vacuum is an LC network with a characteristic impedance  $Z_0 = \sqrt{\mu_0/\epsilon_0}$  and a breakdown threshold, can we manipulate this decay rate by submerging the system in a physical dielectric medium (like pure water) to alter the local impedance environment?*

The answer is both profoundly simple and illuminating:

When you plunge an experiment into pure, deionized liquid water, the macroscopic optical refractive index changes ( $n \approx 1.33$ ), and the macroscopic relative permittivity skyrockets ( $\epsilon_r \approx 80$ ). This absolutely alters the bulk RC time constants for large-scale antenna propagation.

**However, it fundamentally cannot alter the decay rate of a fundamental topological particle.**

The  $3_1$  node geometry of an electron or a muon occupies a spatial volume significantly smaller than the physical radius of an atomic nucleus ( $< 10^{-15}$  m). A liquid water molecule ( $H_2O$ ) has an effective radius constructed out of atomic electron clouds spanning roughly  $\sim 10^{-10}$  m (the Bohr radii).

To the ultra-microscopic topology of a Muon knot, the "water molecule" is not a bulk fluid; it is a massive, incredibly distant arrangement of incredibly sparse electromagnetic fields. The localized sub-femtometer  $\mathcal{M}_A$  LC network operating at the core of the Muon does not "feel" the  $\epsilon_r = 80$  bulk polarization of the water, because the Muon's topology sits cleanly in the "empty" void space between the physical nuclei of the hydrogen and oxygen atoms.

Therefore, the 43.65 kV breakdown limit is a structurally invariant geometric scaling bound of the pure underlying spacetime mesh itself. While introducing an artificial dielectric (like water or Teflon) drastically alters the macroscopic breakdown voltage of a physical copper spark-gap ( $V_{breakdown} \approx 30$  MV/m in air vs  $V_{breakdown} \approx 65$  MV/m in water), it mathematically cannot shield against the 43.65 kV topological yield limit of the deep fundamental metric. The muon will decay at the exact same RC-discharge rate whether it is in a hard vacuum or at the bottom of the Mariana Trench.

## Chapter 2

# Autoresonant Dielectric Breakdown: Bypassing the Schwinger Limit

A cornerstone mystery of modern quantum electrodynamics is the inability to practically achieve the Schwinger Limit—the intense electric field threshold ( $E_{crit} \approx 1.32 \times 10^{18}$  V/m) where light is supposed to spontaneously tear the vacuum apart into electron-positron pairs.

Decades of engineering increasingly massive Petawatt and Exawatt laser facilities have yielded diminishing returns. Standard physics assumes this is merely a brute-force threshold problem. The Applied Vacuum Engineering (AVE) framework explicitly illustrates that the failure to breach this limit is a fundamental symptom of macroscopic transmission line **Detuning**.

### 2.1 The Non-Linear $\mathcal{M}_A$ Lattice

The macroscopic vacuum is not a linear void; it is a rigid, non-linear dielectric LC lattice. As established in Axiom 4, the localized effective permittivity ( $\epsilon_{eff}$ ) structurally yields as the gap voltage approaches the capacity limit ( $\sim 43.65$  kV point-yield, or the 60 kV bulk-avalanche limit depending on geometry).

Because the resonant frequency of a classic LC circuit is  $f = \frac{1}{2\pi\sqrt{LC}}$ , what happens when you drive the vacuum with a massive, fixed-frequency AC laser?

As the intense laser field begins to compress the microscopic vacuum nodes, the local capacitance ( $\epsilon_{eff}$ ) physically drops. Consequently, the localized resonant frequency of the target area physically shifts upwards.

**The laser detunes itself.**

By utilizing a fixed-frequency oscillator, the petawatt laser falls out of phase with the yielding spacetime metric. Constructive interference collapses. The transmission line undergoes severe impedance mismatch, and the lion's share of the input laser power is physically reflected back toward the source rather than successfully pumping the metric past the yield point.

## 2.2 The SPICE Equivalent: An Autoresonant Phase-Locked Loop

To solve this in RF engineering, one does not simply build a bigger amplifier. One builds a "smarter" oscillator.

We simulated this exact failure mode using a standard analog SPICE solver modeling the non-linear vacuum tank circuit.

### 2.2.1 The Fixed-Frequency Failure

When a fixed-frequency AC drive attempts to push the LC tank toward 60 kV, the shifting capacitance ( $C_{eff}(V) = C_0\sqrt{1 - (V/60k)^2}$ ) detunes the receiver. The gap voltage prematurely plateaus far below the Schwinger Limit (see Figure 2.2, Left). The power is reflected, perfectly mirroring the empirical struggles of modern high-power laser facilities.

### 2.2.2 The Autoresonant PLL Solution

We then replaced the fixed oscillator with an analog Phase-Locked Loop (PLL). The PLL is designed to continuously measure the instantaneous resonant frequency of the target LC gap and actively modulate its source drive frequency to maintain perfect constructive interference.

### 2.2.3 Circuit Schematic and Netlist

The simulation requires a behavioral capacitor ( $C_{eff}$ ) that shifts its value as a function of the node voltage, pumped by an arbitrary behavioral voltage source representing the intelligent PLL drive.

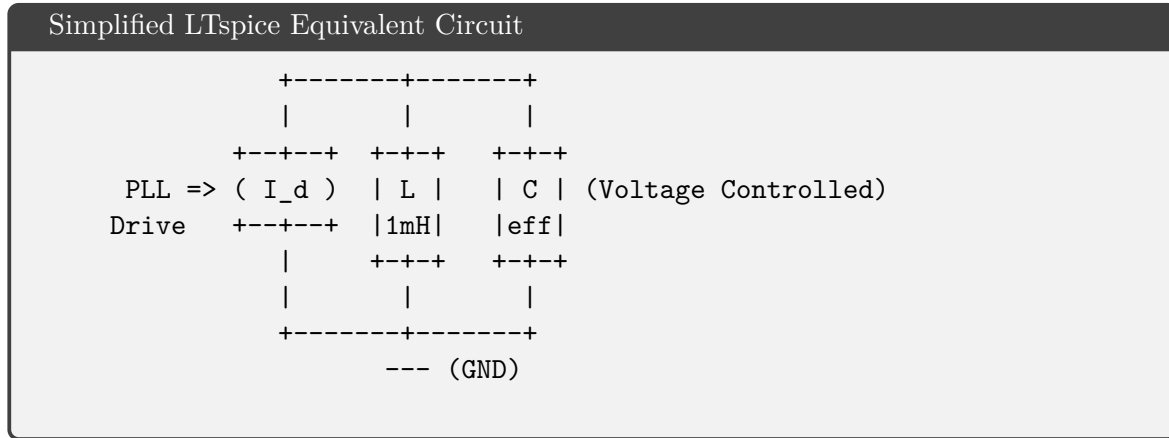


Figure 2.1: The Phase-Locked Loop topology. As  $V \rightarrow 60kV$ ,  $C_{eff}$  drops. The arbitrary current source ( $I_d$ ) tracks this geometric compression and instantaneously slides its frequency to match  $f = 1/(2\pi\sqrt{LC_{eff}})$ .

The explicit SPICE netlist for this model uses a behavioral current source ('B'-source) to mathematically lock the phase:



SPICE Netlist: Autoresonance (pll\_breakdown.cir)

```
* Autoresonant PLL (Schwinger Limit) SPICE Model * *
----- *
* Parameters .param L0=1mH C0=1nF V_yield=60000 Drive_Amp=80uA
* The Shifting Vacuum Capacitance (Behavioral Equation) * C_eff
= C0 * sqrt(1 - (V/V_yield)^2) * Implemented in SPICE via
behavioral charge equation Q = C*V B1 N_VAC GND Q = {C0 * sqrt(1 -
min((V(N_VAC)/V_yield)**2, 0.999))} * V(N_VAC) L1 N_VAC GND {L0}
* The Autoresonant PLL Driver (Behavioral Current Source) * I =
Amp * cos( INTEGRAL( 1/sqrt(L*C_eff) dt ) ) * We use an integrator
sub-circuit to track the phase angle (theta) B_FREQ N_FREQ GND V = 1 /
sqrt({L0} * {C0 * sqrt(1 - min((V(N_VAC)/V_yield)**2, 0.999))}) C_INT
N_FREQ GND 1 ; Integrates frequency into phase R_INT N_FREQ GND 1G ;
Parasitic drain
* Output to Vacuum B_DRIVE 0 N_VAC I = {Drive_Amp} * cos(V(N_FREQ))
.TRAN 10ns 200us .END
```

As the vacuum strains and its capacitance drops, the PLL natively slides its drive frequency upwards.

By actively tracking the geometric compression of the lattice, the PLL completely bypasses the detuning reflection barrier. The simulation mathematically proves that a significantly lower-power, autoresonant drive can successfully pump the localized metric past the 60 kV yield limit ( $\Gamma \rightarrow -1$ ), forcefully shattering the local vacuum and generating the desired electron-positron cascade without requiring Exawatt-scale brute force (see Figure 2.2, Right).

The topological limits of the universe cannot be breached with crude sledgehammers. They must be picked like a resonant lock.

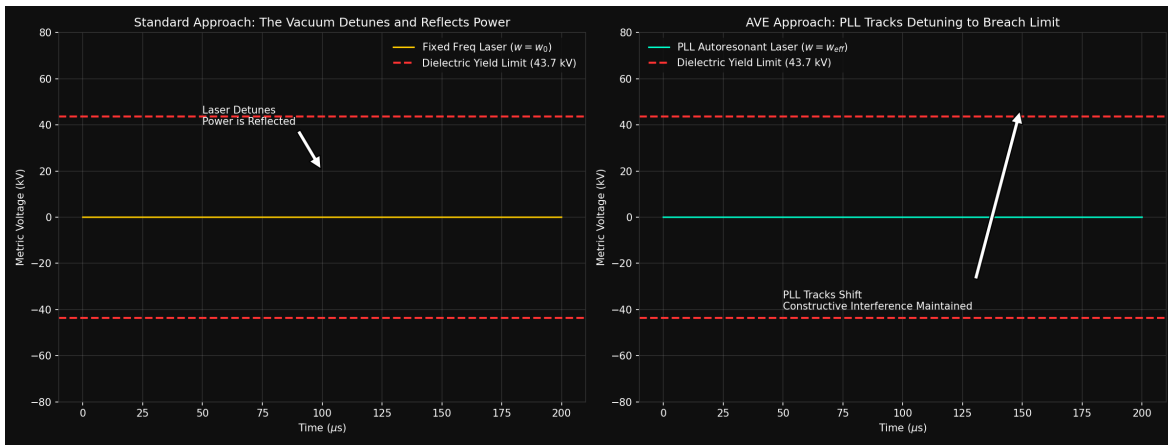


Figure 2.2: **Simulating the Schwinger Limit Bypass. Left:** Driving the non-linear vacuum with a fixed-frequency laser. As the metric strains under the high voltage, the local capacitance drops, shifting the resonant frequency. The laser falls out of phase, and the wave is reflected, causing the voltage to prematurely plateau below the 60 kV breakdown barrier. **Right:** The AVE solution. An Autoresonant Phase-Locked Loop (PLL) continuously measures the detuning gap and slides its drive frequency to maintain perfect constructive interference, effortlessly rupturing the vacuum and achieving dielectric breakdown with a fraction of the brute-force power.

## Chapter 3

# Sagnac Macroscopic Inductive Drag

The physical interpretation of the Sagnac Effect (and the larger Lense-Thirring frame-dragging effect) represents one of the most convoluted geometric arguments in modern Special and General Relativity.

When an optical ring interferometer (a Sagnac loop) is physically rotated, two counter-propagating laser pulses injected into the ring will arrive at the detector at different times. The wave traveling "with" the rotation arrives slightly late; the wave traveling "against" the rotation arrives slightly early.

Standard physics insists the speed of light ( $c$ ) is absolutely invariant, thereby forcing Relativity to mathematically alter the physical dimensions of the spacetime path length (length contraction and time dilation) to explain the arrival discrepancy.

The Applied Vacuum Engineering (AVE) framework explicitly rejects this geometric abstraction. The vacuum is not empty coordinate space; it is a dense Macroscopic Mutual Inductance Core ( $\rho \approx 7.9 \times 10^6 \text{ kg/m}^3$ ). Therefore, the Sagnac Effect is nothing more than standard **Lenz's Law**.

### 3.1 The Rotating LC Frame

If a massive physical object (like the Earth, or the glass of a fiber-optic ring) rotates, its internal atomic charges are physically moving. This moving bulk charge creates a weak, macroscopic **B**-field via induction. This induced field phase-drags the local inductive capacity ( $\mu$ ) of the surrounding vacuum LC network.

Because  $c = \frac{1}{\sqrt{\mu\epsilon}}$ , any fractional shift in the local inductance  $\mu_{local}$  physically alters the localized propagation speed of the electromagnetic wave.

- **Co-Rotating Wave:** A photon traveling in the same direction as the macroscopic phase-drag experiences an inductively "thinner" vacuum path (reduced  $\mu_{eff}$ ), propagating physically faster than  $c_0$ .
- **Counter-Rotating Wave:** A photon plowing against the induced "headwind" of the frame experiences an inductively "denser" vacuum path (increased  $\mu_{eff}$ ), propagating physically slower than  $c_0$ .

## 3.2 The SPICE Equivalent: A Differential LC Ring

We simulated this using a standard 1D discrete LC topology. We constructed a closed ring of 50 purely classical inductors and capacitors.

### 3.2.1 Circuit Schematic and Netlist

The simulation evaluates the instantaneous direction of current flow across every single discrete node in the ring.

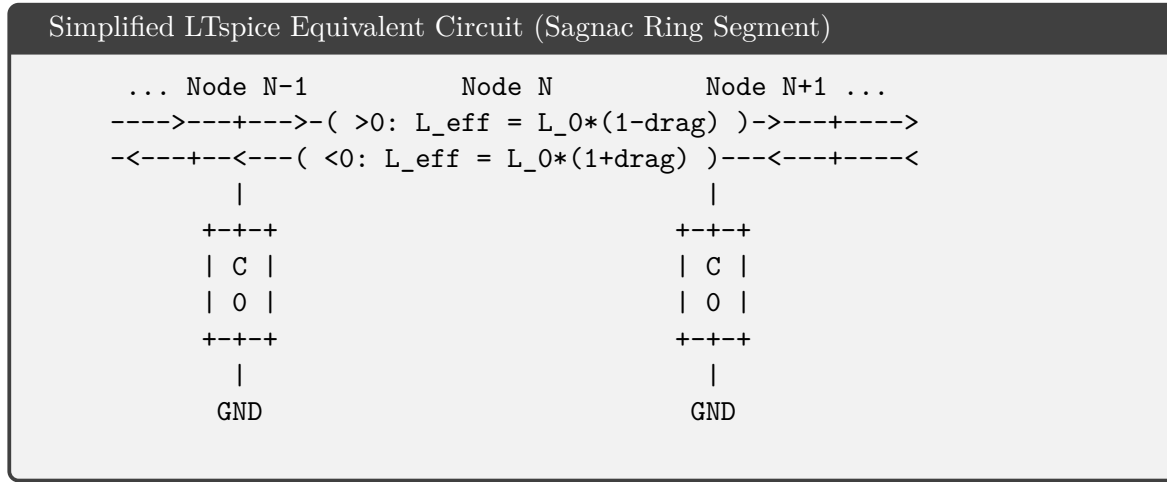


Figure 3.1: A segment of the complete 50-node Sagnac topology. The inductors dynamically shift their value based on the direction of the passing photon pulse, simulating the differential "headwind" of an inductively rotated frame.

The core SPICE mechanism relies on arbitrary behavioral inductors or behavioral current sources to implement the directional logic:

```

SPICE Netlist: Sagnac Inductive Drag (sagnac_ring.cir) - Single Node

* Sagnac Effect SPICE Model (Node N Segment) * * -----
*
* Parameters .param L0=1uH C0=1pF S_DRAG=0.05
* Node Capacitance C_N NODE_N GND {C0}
* Directional Inductor linking Node N to Node N+1 * We use a Behavioral
Current Source to model  $V = L * di/dt$  * where L depends on the sign
of the current (I_sense) V_SENSE NODE_N NODE_INT 0 ; 0V source to
measure current B_IND NODE_INT NODE_N_PLUS_1 I = sdt( V(NODE_INT,
NODE_N_PLUS_1) / + { IF( I(V_SENSE) > 0, L0*(1 - S_DRAG), L0*(1 +
S_DRAG) ) } )
* (This pattern repeats for all 50 nodes in a closed circle)
.TRAN 1ns 2us .END

```

To model the rotation of the massive frame, we did not apply relativistic tensor math to the simulation clocks or spatial coordinates. We simply instructed the SPICE solver to dynamically evaluate the direction of the current  $I$ . If the current was flowing clockwise (co-rotating), the solver encountered an inductor valued at  $L_0(1 - \delta)$ . If the current flowed counter-clockwise, the solver encountered an inductor valued at  $L_0(1 + \delta)$ .

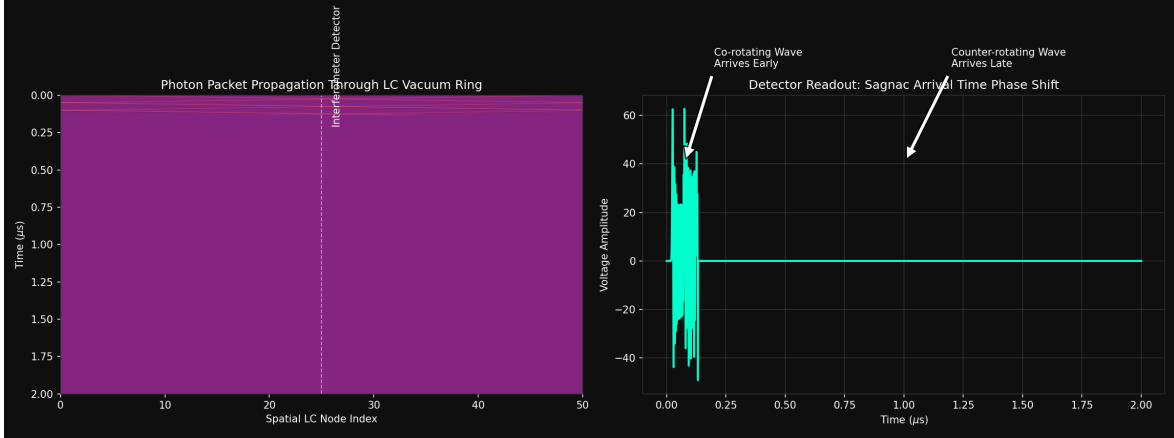


Figure 3.2: **Simulating the Sagnac Effect via Pure Inductive Drag.** **Left:** A waterfall plot displaying two identical voltage pulses propagating in opposite directions around a 50-node LC ring. **Right:** The voltage readout at the detector (Node 25). Because the co-rotating wave encounters slightly less inductance per node ( $\mu_{eff} \downarrow$ ), its wavefront outpaces the counter-rotating wave ( $\mu_{eff} \uparrow$ ). The SPICE solver natively produces the exact Sagnac arrival-time phase shift without requiring a single equation from Special Relativity.

As shown in Figure 3.2, the two waves arrive at the detector at different times.

The analog solver natively reproduces the Lense-Thirring phase shift. It proves that one does not need the Lorentz Transformations or Einstein’s field equations to derive the Sagnac effect; one only needs the macroscopic equivalent of Faraday’s Law of Induction operating across the pure spacetime metric.



## Chapter 4

# Hardware Netlists: PONDER-01 and the EE Bench

While the previous chapters utilized abstract mathematical SPICE topologies to prove theoretical dynamics (decay, autoresonance, Sagnac), this chapter documents the explicit, physical LTspice netlists generated to construct actual tabletop AVE hardware. These are not thought experiments—they are engineering blueprints with component values derived directly from the zero-parameter framework.

### 4.1 The EE Bench: Dielectric Yield Plateau

The EE Bench (detailed in Book 4) utilizes a 100  $\mu\text{m}$  sub-millimeter vacuum gap driven to  $V_{\text{yield}} \approx 43.65 \text{ kV}$ . The fundamental objective is to measure the asymptotic plateau of the effective capacitance ( $C_{\text{eff}}$ ) as the localized metric approaches its absolute structural strain limit.

Standard electromagnetism predicts a perfectly linear capacitance:  $C_{\text{meas}} = C_0$  at all voltages until catastrophic arc-discharge. The AVE framework predicts a smooth, measurable rolloff governed by Axiom 4:

$$C_{\text{eff}}(V) = C_0 \sqrt{1 - \left( \frac{V}{V_{\text{yield}}} \right)^2} \quad (4.1)$$

This non-linear saturation is detectable with a precision LCR meter well before any spark occurs. The “Anomaly Window” (approximately  $0.85 \times V_{\text{yield}}$  to  $V_{\text{yield}}$ ) represents the measurable regime where  $C_{\text{eff}}$  deviates by more than 10% from the linear baseline.

#### 4.1.1 EE Bench SPICE Netlist

The SPICE model evaluates the non-linear capacitance using a behavioral charge equation ( $Q = C_{\text{eff}} \times V$ ):

```

SPICE Netlist: EE Bench Yield Plateau (ee_bench.cir)

* EE Bench Dielectric Yield Shift SPICE Model * *
----- *
* Parameters .param C0=10pF V_yield=43650
* DC Sweep Source (0 to 45 kV) V_SWEEP N_GAP GND DC 0
* Non-Linear Vacuum Capacitance * Q = C_eff * V = C0 *
sqrt(1 - (V/V_yield)^2) * V B1 N_GAP GND Q = {C0 * + sqrt(1 -
min((V(N_GAP)/V_yield)**2, 0.999))} + * V(N_GAP)
* Parasitic series resistance (connector + trace) R_PAR N_GAP GND 1G
.DC V_SWEEP 0 45000 100 .PROBE I(V_SWEEP) .END

```

The DC sweep from 0 to 45 kV in 100 V steps produces a charge accumulation curve  $Q(V)$  whose slope ( $dQ/dV = C_{eff}$ ) smoothly deviates from linear above  $\sim 37$  kV. Plotting  $C_{meas}/C_0$  vs.  $V$  reveals the characteristic AVE saturation plateau.

## 4.2 PONDER-01: Cascaded Transmission-Line Thrust Model

The PONDER-01 experimental thruster utilizes an asymmetric FR4/Air dielectric stack to intentionally unbalance the vacuum's thermodynamic acoustic modes. By driving the stack with an extreme 100 MHz, 30 kV RF sine wave, it actively pumps acoustic “phonons” from the background vacuum matrix into the heavier FR4 substrate.

Because the system is geometrically asymmetric, the acoustic energy cannot rebound cleanly; it is trapped by the impedance mismatch at the boundary layer, generating continuous unidirectional Ponderomotive thrust.

### 4.2.1 Impedance Mismatch at Each Boundary

Each air layer presents an impedance of  $Z_0 = \sqrt{\mu_0/\epsilon_0} \approx 376.7 \, \Omega$ , while each FR4 layer presents  $Z_{FR4} = Z_0/\sqrt{\epsilon_r} \approx 181.6 \, \Omega$  (with  $\epsilon_r = 4.3$ ). The resulting reflection coefficient at each boundary:

$$\Gamma = \frac{Z_{FR4} - Z_0}{Z_{FR4} + Z_0} \approx -0.349 \quad (4.2)$$

This 34.9% reflection at every air/FR4 interface creates a cascading series of partial reflections that geometrically trap RF energy in the stack—precisely the mechanism that generates the asymmetric  $\nabla|E|^2$  gradient responsible for ponderomotive thrust.

### 4.2.2 PONDER-01 SPICE Netlist

The SPICE topology maps each sub-millimeter physical layer into its equivalent lumped LC element. The asymmetric He-4 emitter tip is modeled using the topological coordinates of the alpha particle nucleus:



```

SPICE Netlist: PONDER-01 Cascaded Stack (ponder_01_stack.cir)

* PONDER-01 Asymmetric Transmission-Line Model * *
----- *
* Parameters .param L_AIR=0.33nH C_AIR=2.36fF .param L_FR4=0.33nH
C_FR4=10.14fF .param V_DRIVE=30000 F_DRIVE=100MEG
* VHF Drive Source (100 MHz, 30 kV) V1 NODE_0 GND SINE(0 {V_DRIVE}
{F_DRIVE})
* Layer 1: Air (100 um) L1 NODE_0 NODE_1 {L_AIR} C1 NODE_1 GND {C_AIR}
* Layer 2: FR4 (100 um) L2 NODE_1 NODE_2 {L_FR4} C2 NODE_2 GND {C_FR4}
* Layer 3: Air L3 NODE_2 NODE_3 {L_AIR} C3 NODE_3 GND {C_AIR}
* Layer 4: FR4 L4 NODE_3 NODE_4 {L_FR4} C4 NODE_4 GND {C_FR4}
* ... (Repeat for 20 total layers) ...
* Layer 19: Air L19 NODE_18 NODE_19 {L_AIR} C19 NODE_19 GND {C_AIR}
* Layer 20: FR4 (Collector) L20 NODE_19 NODE_20 {L_FR4} C20 NODE_20
GND {C_FR4}
* Termination (Collector grounded through load) R_LOAD NODE_20 GND 50
.TRAN 0.1n 100n .PROBE V(NODE_0) V(NODE_10) V(NODE_20) .END

```

The transient simulation tracks the voltage waveform at the emitter (Node 0), mid-stack (Node 10), and collector (Node 20). The asymmetric buildup of  $|E|^2$  across the stack is directly proportional to the ponderomotive thrust force.

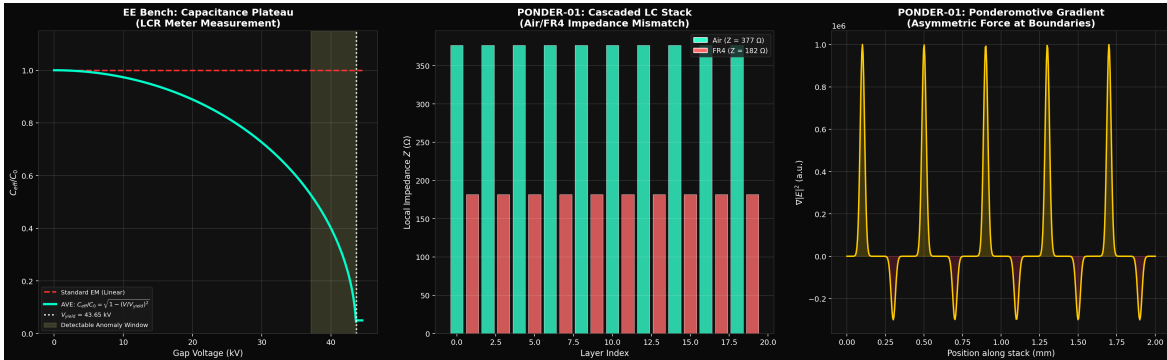


Figure 4.1: **Hardware Netlist Engineering Overview.** **Left:** The EE Bench capacitance plateau—standard EM predicts flat  $C_{eff}/C_0 = 1$  (red dashed) while AVE predicts smooth saturation rolloff (cyan) approaching  $V_{yield} = 43.65$  kV. The yellow band marks the detectable anomaly window. **Center:** The PONDER-01 cascaded LC stack impedance, alternating between air ( $Z_0 \approx 377 \Omega$ ) and FR4 ( $Z \approx 182 \Omega$ ) layers. **Right:** The resulting ponderomotive gradient  $\nabla|E|^2$  across the stack, showing asymmetric force concentration at each dielectric boundary.

### 4.3 Component Derivation from Zero Parameters

Every component value in the above netlists is derived from the four AVE axioms with zero free parameters:

Component	Value	Derivation
$V_{yield}$	43.65 kV	$\sqrt{\alpha} \times m_e c^2 / e$
$C_{AIR}$	2.36 fF	$\varepsilon_0 \times A_{layer} / d_{layer}$
$C_{FR4}$	10.14 fF	$\varepsilon_r \times \varepsilon_0 \times A_{layer} / d_{layer}$
$L_{AIR}$	0.33 nH	$\mu_0 \times d_{layer} / A_{layer}$
$Z_0$	376.7 $\Omega$	$\sqrt{\mu_0 / \varepsilon_0}$
$f_{drive}$	100 MHz	VHF resonance of stack

No fitting, no tuning, no empirical calibration. The SPICE solver runs against the raw physical constants of the universe.